Electrical Switching of Tristate Antiferromagnetic Néel Order in α-Fe$_2$O$_3$ Epitaxial Films

Yang Cheng,[1,*] Sisheng Yu,[1,*] Menglin Zhu,[2] Jinwoo Hwang,[2] and Fengyuan Yang[1]

[1]*Department of Physics, The Ohio State University, Columbus, Ohio 43210, USA*
[2]*Department of Materials Science and Engineering, The Ohio State University, Columbus, Ohio 43212, USA*

We demonstrate nondecaying, steplike electrical switching of tristate Néel order in Pt/α-Fe$_2$O$_3$ bilayers detected by the spin-Hall induced anomalous Hall effect. The as-grown Pt/α-Fe$_2$O$_3$ bilayers exhibit sawtooth switching behavior generated by current pulses. After annealing by a high pulse current, the Hall signals reveal single-pulse saturated, nondecaying, steplike switching. Together with control experiments, we show that the sawtooth switching is due to an artifact of Pt while the actual spin-orbit torque induced antiferromagnetic switching is steplike. Our Monte Carlo simulations explain the switching behavior of α-Fe$_2$O$_3$ Néel order among three in-plane easy axes.

Spin-orbit torque (SOT) induced switching of ferromagnets (FM) by an adjacent heavy metal (HM) has raised wide interest in recent years [1–3], where a charge current in the HM generates spins at the HM/FM interface via the spin Hall effect (SHE). Antiferromagnets (AFMs) offer the advantage of no stray field, robustness against an external field, a THz response, and an abundance of material selections [4–12]. It has been predicted that Néel SOT can be utilized to switch AFM spins in picoseconds for THz operations [13–17]. Electrical switching of bistate AFM moments has been demonstrated in metallic AFMs, CuMnAs and Mn$_2$Au [18–22]. For antiferromagnetic insulators (AFIs), the switching of Néel order can be achieved in HM/AFI bilayers by dampinglike SOT, as shown recently in Pt/NiO bilayers with sawtooth shaped switching, which was interpreted as that every ~1 ms current pulse can flip the AFM-Néel order incrementally [23–26]. In this Letter, we report the first observation of tristate, steplike switching of Néel order in Pt(2 nm)/α-Fe$_2$O$_3$(30 nm) bilayers grown on Al$_2$O$_3$(001) substrates, which is read out by Hall resistance (ΔR_{xy}) detection. Our results demonstrate that the sawtooth ΔR_{xy} is an artifact from the Pt layer, while the SOT-induced AFM switching is steplike.

Epitaxial α-Fe$_2$O$_3$ films are grown on Al$_2$O$_3$(001) substrates using off-axis sputtering, [27–29] followed by *in situ* deposition of a Pt layer on α-Fe$_2$O$_3$ at room temperature [30,31]. α-Fe$_2$O$_3$ is a high temperature AFI with a corundum structure as shown in Fig. 1(a). The Fe^{3+} moments stay in the (001) plane and stack antiferromagnetically along the c axis above the Morin transition temperature [32,33] (see Supplemental Material [34], which includes Refs. [35–38]). Figure 1(b) shows a $2\theta/\omega$ x-ray diffraction (XRD) scan of an α-Fe$_2$O$_3$(30 nm) epitaxial film on Al$_2$O$_3$(001), where the Laue oscillations of the α-Fe$_2$O$_3$(006) peak in the inset indicate its high quality. The scanning transmission electron microscopy (STEM) image

of a Pt(2 nm)/α-Fe$_2$O$_3$(30 nm) bilayer shown in Fig. 1(c) reveals the single-crystalline ordering of α-Fe$_2$O$_3$ and the clean Pt/Fe$_2$O$_3$ interface.

Figure 2(a) shows the ab plane of the α-Fe$_2$O$_3$ hexagonal lattice with three easy axes along [210], [120], and [1$\bar{1}$0]
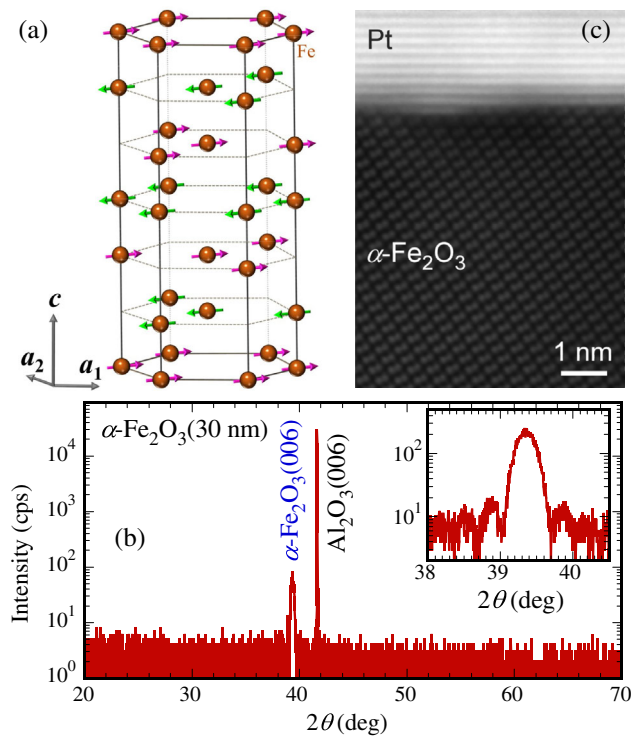

FIG. 1. (a) Schematic of the α-Fe$_2$O$_3$ hexagonal lattice with FM-aligned Fe moment in the ab plane and AFM coupling between adjacent ab planes (oxygen atoms not shown). (b) $2\theta/\omega$ XRD scan of a 30 nm α-Fe$_2$O$_3$ epitaxial film on Al$_2$O$_3$(001). The inset shows an enlarged region around the α-Fe$_2$O$_3$(006) peak. (c) STEM image of a Pt(2 nm)/α-Fe$_2$O$_3$(30 nm) bilayer.
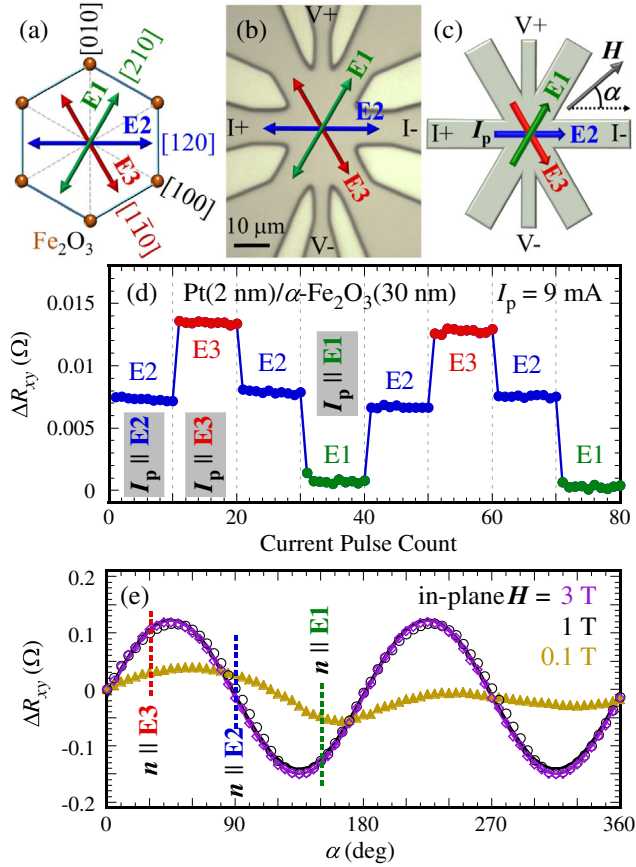
FIG. 2. (a) The *ab* plane of an α-Fe$_2$O$_3$ lattice with three in-plane easy axes, [210], [120], and [1$\bar{1}$0] labeled as **E1**, **E2**, and **E3**, resulting in a triaxial anisotropy, where the double arrows represent the AFM spins. (b) Optical microscopy image and (c) schematic of an eight-leg Hall cross of a Pt(2 nm)/α-Fe$_2$O$_3$(30 nm) bilayer, where α is the angle between an in-plane field and the **E2** direction. (d) A sequential pulse current of $I_p = 9$ mA is applied along one of the three easy axes (10 pulses for each segment) at 300 K and a reversible control of the tristate Hall resistance is detected by applying a 0.1 mA sensing current along **E2**. (e) In-plane α dependence of ΔR_{xy} at $H = 0.1$, 1, and 3 T, where ΔR_{xy} saturates at $H \geq 1$ T. The gray and purple solid curves are $\sin 2\alpha$ fits.

[32,39]. We pattern our Pt(2 nm)/α-Fe$_2$O$_3$(30 nm) bilayers into 8-leg Hall crosses, as shown in Figs. 2(b) and 2(c), where the width of the two vertical Hall terminals is 5 μm and the other six legs (60° apart) are 10 μm wide. We determine the crystallographic axes of the samples using reflection high-energy electron diffraction (RHEED) to align **E1**, **E2**, and **E3** with the [210], [120], and [1$\bar{1}$0] easy axes of α-Fe$_2$O$_3$, respectively (see Supplemental Material [34]).

Hall resistances of the patterned bilayers are measured using a physical property measurement system (PPMS) at 300 K unless specified otherwise. During our switching measurements, we first apply a 1-ms pulse current (I_p) along one of three easy axes, wait for 30 sec, and then measure the Hall voltage across the two vertical terminals by sending a small sensing current (I_s) of 100 μA along **E2**. After a series of 10 pulses, we change the direction of I_p to another easy axis and repeat the measurement. Figure 2(d) shows ΔR_{xy} as a function of the pulse count at $I_p = 9$ mA (current density, $j = 4.5 \times 10^7$ A/cm^2), which exhibits clean tristate Hall resistances at $I_p \| \textbf{E1}$ (low), $I_p \| \textbf{E2}$ (intermediate), and $I_p \| \textbf{E3}$ (high) as I_p is switched from **E2** → **E3** → **E2** → **E1** → **E2**. This switching behavior can be understood as follows: (i) when an initial pulse current is applied along one of the three easy axes, the dampinglike SOT rotates the Néel order n to align with I_p [23], (ii) a small sensing current is sent along **E2** and a spin-Hall induced anomalous Hall effect (SH-AHE) voltage is measured, which reflects the orientation of n, (iii) after the first pulse, the subsequent 9 pulses cause essentially no change in n, resulting in a plateau, and (iv) as I_p is changed to a new easy axis, n aligns with the new direction of I_p, leading to a step jump of ΔR_{xy}. The steplike switching of the Néel order is in distinct contrast with previous reports in Pt/NiO bilayers with sawtooth shaped ΔR_{xy}.

The magnitude of the Hall resistance, $\Delta R_{xy}(\textbf{E3}) > \Delta R_{xy}(\textbf{E2}) > \Delta R_{xy}(\textbf{E1})$ arises from the relative angle of $-60°$, $0°$, and $+60°$ between n and I_s (which generate spins $\sigma \perp I_s$ in Pt vis SHE) for I_p along **E3**, **E2**, and **E1**, respectively, as expected from the angular dependence of the dampinglike SOT induced SH-AHE [23,26,40]. To corroborate the results in Fig. 2(d), we use an independent approach to control the Néel order by an applied field (H) which aligns $n \perp H$ via the in-plane spin-flop (SF) transition once H exceeds the SF field. Figure 2(e) shows the angular dependence of ΔR_{xy} by applying an in-plane field [see Fig. 2(c) where α is the angle between H and **E2** or [120] crystal axis] of 0.1, 1, and 3 T, which is analogous to the planar Hall measurement in FMs. At $H \geq 1$ T, ΔR_{xy} reaches saturation and follows $\sin 2\alpha$, while at $H = 0.1$ T it shows an irregular angular dependence, indicating that the in-plane SF transition in our α-Fe$_2$O$_3$ films occurs at below 1 T with $n \perp H$ [40,41]. The peak-to-valley magnitude of ΔR_{xy} in Fig. 2(e) is 0.27 Ω, which gives the upper limit of Hall resistance change in Pt/α-Fe$_2$O$_3$ switching measurement. The plateaus in Fig. 2(d) for **E3**, **E2**, and **E1** correspond to $\alpha = 30°$, $90°$, and $150°$ marked in Fig. 2(e), respectively. The values of ΔR_{xy} in Fig. 2(d) are smaller as compared to the corresponding points in Fig. 2(e), and we will explain it below in Fig. 4.

Because for dampinglike SOT $\propto n \times (j \times \hat{z}) \times n$, the magnitude of pulse current density j determines ΔR_{xy} [23], we measure the I_p dependence of the Pt/α-Fe$_2$O$_3$ samples by applying I_p along **E1** and **E3**, as shown in Fig. 3(a). As I_p increases, ΔR_{xy} changes from single-pulse saturation, steplike switching to sawtooth shaped switching. At $I_p = 16$ mA, there is a clear decay of ΔR_{xy} after several
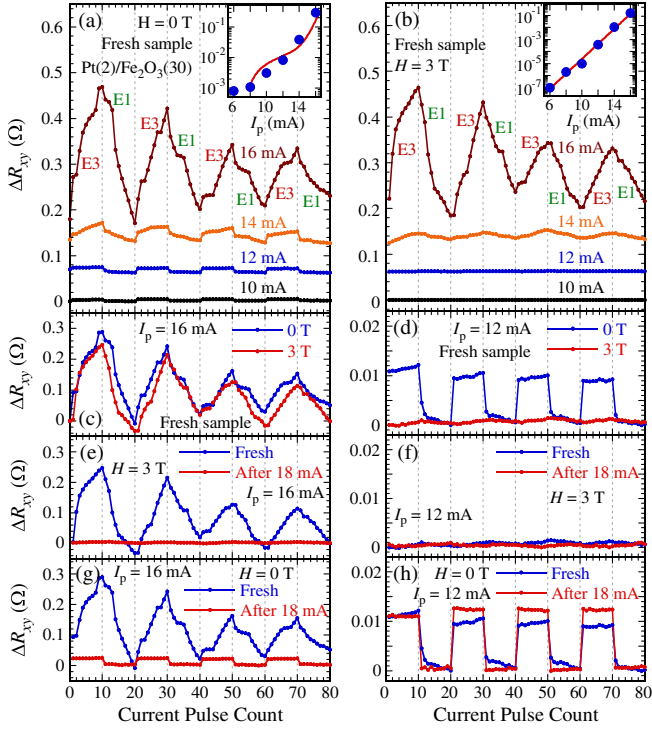
FIG. 3. Evolution of ΔR_{xy} when the pulse current is switched between E3 and E1 (10 pulses each) under (a) 0 and (b) 3 T in-plane field applied perpendicular to **E2** for a Pt(2 nm)/α-Fe$_2$O$_3$(30 nm) bilayer. Insets: semilog plots of ΔR_{xy} vs I_p. The red line in inset (b) is an exponential fit, $y = (1.38 \times 10^{-11})e^{1.44x}$, and the red curve in inset (a) is given by $y = (1.38 \times 10^{-11})e^{1.44x} + (-0.0183 + 0.00243x)$, which is the sum of the exponential fit in inset (a) here and the linear fit in Fig. 4(c). Comparison of ΔR_{xy} at 0 and 3 T with (c) $I_p = 16$ and (d) $I_p = 12$ mA for a fresh sample. Comparison of ΔR_{xy} for a fresh sample and the same sample after 18 mA annealing at (e) $I_p = 16$ in a 3 T in-plane field ($H\perp$**E2**), (f) $I_p = 12$ at 3 T, (g) $I_p = 16$ at 0 T, and (h) $I_p = 12$ mA at 0 T.

cycles of pulses. During the first cycle, ΔR_{xy} is ~ 0.3 Ω, which is above the upper limit of 0.27 Ω given by Fig. 2(e). The obvious decay at $I_p = 16$ mA has been observed in other HM/AFI switching systems, which was attributed to the decrease of switching efficiency [19,24].

To uncover the cause of sawtooth switching and the decay of ΔR_{xy}, we perform the same measurement using another Hall cross on the same sample in an in-plane field of 3 T applied at $H\perp$**E2** [Fig. 3(b)]. Since H is fixed at $\alpha = 90°$ and above the SF field, the AFM moments are frozen along **E2** and no switching is expected. Surprisingly, the 3 T field has essentially no impact on ΔR_{xy} at $I_p = 16$ mA, which remains sawtoothlike with similar magnitude. The 12 and 10 mA curves, on the other hand, show sharp differences, becoming flat lines (no switching) in Fig. 3(b). The inset in Fig. 3(b) plots ΔR_{xy} vs I_p in a semilog scale, exhibiting an exponential dependence. Likewise, the inset in Fig. 3(a) shows a similar plot for 0 T, where the red
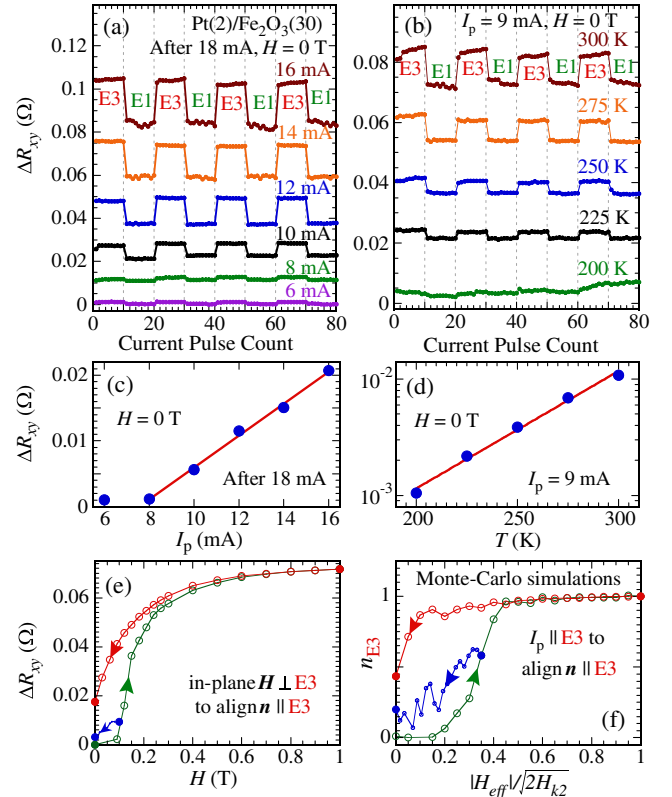

FIG. 4. (a) Pulse current dependence of ΔR_{xy} for a Pt(2 nm)/α-Fe$_2$O$_3$(30 nm) bilayer when I_p is switched between **E3** and **E1** (10 pulses each) measured at 300 K. (b) Temperature dependence of ΔR_{xy} (between **E3** and **E1**) at $I_p = 9$ mA. All measurements here are taken on a sample after 18 mA annealing. (c) ΔR_{xy} vs I_p from (a), showing a linear dependence (red fitting line: $y = -0.0183 + 0.00243x$). (d) Semilog plot of ΔR_{xy} vs T for $I_p = 9$ mA from (b), indicating an exponential dependence. (e) In-plane field dependence of ΔR_{xy} with $H\perp$**E3** [$\alpha = 30°$, see Fig. 2(c)], which tends to align $n\parallel$**E3**. The field is ramped from 0 to 1 T (green), then back to 0 T (red), which corresponds to a first-quadrant full hysteresis loop. In a separate scan, H is ramped from 0 to 0.1 T (green), then back to 0 T (blue), corresponding to a minor hysteresis loop. (f) Monte Carlo simulations of the full and minor hysteresis loops of the component of n along **E3** (n_{E3}) as a function of the effective magnetic field due to SOT generated by a pulse current $I_p\parallel$**E3**, which agrees with the experimental data in (e).

curve is not a fit, but the sum of exponential fit obtained in the inset of Fig. 3(b) and the linear fit from Fig. 4(c) below.

To highlight the contrast between Figs. 3(a) and 3(b), Figs. 3(c) and 3(d) show the comparison of ΔR_{xy} between the 0 and 3 T data at $I_p = 16$ and 12 mA, respectively. In Fig. 3(c) for $I_p = 16$ mA, there is essentially no difference between the 0 and 3 T curves despite the different AFM spin configurations. In Fig. 3(d) for $I_p = 12$ mA, the 3 T field turns the steplike ΔR_{xy} at 0 T into an essentially flat line (with a very small but non-negligible sawtooth shape), suggesting that the steplike switching is the real AFM switching while the sawtooth feature has a different origin.

Considering the sawtooth feature is most obvious at $I_p = 16$ mA, we apply an even higher pulse current of 18 mA ($j = 9.0 \times 10^7$ A/cm^2) at zero field to anneal the 2 nm Pt layer and then redo the measurement at $I_p = 16$ and 12 mA in a 3 T field, as shown in Figs. 3(e) and 3(f), respectively. In both cases, there is no switching and ΔR_{xy} remains flat after the annealing. We next perform the same measurement at zero field for $I_p = 16$ and 12 mA. Figure 3(g) shows that after the annealing, the sawtooth curve at $I_p = 16$ mA is transformed to a steplike switching. In Fig. 3(h) for $I_p = 12$ mA, ΔR_{xy} remains steplike while the switching becomes more squarelike. This result demonstrates that the annealing dramatically changes the detected switching behavior, which we attribute to the improved stability of the Pt(2 nm) layer after the annealing.

Since the switching of Pt/α-Fe$_2$O$_3$ samples becomes significantly more stable after the annealing, we can obtain a reliable I_p dependence of the SOT-induced switching. Figure 4(a) shows that for the whole current range from 6 to 16 mA, ΔR_{xy} exhibits steplike switching with high stability and no detectable decay. The onset of switching occurs at $I_p = 6$ mA or $j = 3.0 \times 10^7$ A/cm^2, comparable to the values for typical HM/FM systems [2,3]. A linear-scale plot of ΔR_{xy} vs I_p shown in Fig. 4(c) exhibits a linear dependence at $I_p \geq 8$ mA. This indicates the SOT responsible for the AFM switching is linearly proportional to the magnitude of I_p, which in turn is proportional to the SHE-generated spin accumulation at the Pt/α-Fe$_2$O$_3$ interface. In addition, the fitting parameters obtained from Fig. 4(c), together with the exponential fitting to the inset in Fig. 3(b), are used to create the red curve in the inset in Fig. 3(a), which approximately agrees with the experimental data for fresh samples without the annealing.

During the switching of n from one easy axis to another, thermal fluctuation is expected [19,26] to help n overcome the potential barrier due to magnetocrystalline anisotropy. We measure the temperature (T) dependence of ΔR_{xy} at $I_p = 9$ mA from 200 to 300 K at zero field as shown in Fig. 4(b), which decreases at lower temperatures as expected. Figure 4(d) shows the ΔR_{xy} vs T plot, which exhibits an exponential dependence, confirming thermally activated AFM switching [19].

Figure 4(e) shows the dependence of ΔR_{xy} on the magnitude of an in-plane field applied at $H \perp \mathbf{E3}$, [$\alpha = 30°$, see Fig. 2(c)], which aligns $n \| \mathbf{E3}$ at H above the SF field. As H is ramped from 0 to 1 T (initial curve) and then back to 0 T, the ΔR_{xy} vs H curve exhibits a full loop in the first quadrant, analogous to FMs. The remanence of ΔR_{xy} at $H = 0$ T on the red curve is ~25% of the saturation value at 1 T because the α-Fe$_2$O$_3$ film transitions from a single domain to multidomains as H is reduced to below the SF field. We also perform a minor loop measurement by ramping H from 0 to 0.1 T and then

back to 0 T, which exhibits a much smaller remanence at 0 T.

A pulse current applied along an easy axis generates SHE-induced spin accumulation near the Pt/α-Fe$_2$O$_3$ interface, which acts as an effective magnetic field $\propto (j \times \hat{z}) \times n$ and exerts a SOT on the Néel order to align n with I_p. This is similar to a FM whose magnetization can be aligned by a magnetic field. Given the THz response of AFMs [13] and that the sample temperature can be stabilized in μs [19], a single 1-ms pulse is long enough for an AFM to reach equilibrium. As a result, the percentage of Néel order switching only depends on the magnitude of I_p rather than the number of pulses. Since our ΔR_{xy} is recorded using a small sensing current long after the pulse current is off, the measured signal is the remanence of ΔR_{xy}, which is a fraction of the saturation value. This is analogous to the demagnetization process of FMs and can explain why ΔR_{xy} in switching measurements is much smaller than that in the field-dependence measurements shown in Fig. 2(e).

Figure 4(f) shows our Monte Carlo simulations of the full and minor loops in Fig. 4(e) by computing the component of n along **E3**, $n_{\mathbf{E3}}$, as a function of the effective magnetic field, $H_{\text{eff}}/\sqrt{2H_{k2}}$, generated by the SOT with $I_p \| \mathbf{E3}$, where H_{k2} is the easy-plane anisotropy field (see Supplemental Material [34] for details). The simulation result of SOT-induced switching qualitatively agrees with the experimental result in Fig. 4(e) induced by an external field, revealing the similarities in the control of AFM spins between a magnetic field and current-induced SOT.

To uncover the reason for the sawtooth switching, we perform the switching measurements for a Pt(2 nm) film directly deposited on Al$_2$O$_3$ and SrTiO$_3$ (see Supplemental Material [34]), which display the sawtooth shaped ΔR_{xy}. We speculate that the sawtooth feature of ΔR_{xy} is due to the current-driven migration of grain boundaries in thin Pt layers. This proves that the sawtooth feature is an artifact [42] due to Pt and not related to the AFM switching, while the actual AFM switching exhibits single-pulse saturation, steplike Hall resistance, which disappears after the AFM spins are "frozen" by a magnetic field. As a comparison, we also try electrical switching of a Pt/Cr$_2$O$_3$ bilayer (see Supplemental Material [34]), which does not exhibit AFM switching because the Cr$_2$O$_3$ epitaxial film is an AFM with an out-of-plane uniaxial anisotropy. Our results point to a promising path toward controlling AFM spins in insulating AFMs using spin-orbit torque. Also, we proposed a criterion to separate the SOT switching from the artifacts, where a real AFM switching is unattenuated and can be suppressed by a magnetic field when exceeding the spin-flop field.

---

*These authors contributed equally to this work.

[1] L. Q. Liu, C. F. Pai, Y. Li, H. W. Tseng, D. C. Ralph, and R. A. Buhrman, Spin-torque switching with the giant spin Hall effect of tantalum, Science **336,** 555 (2012).

[2] L. Q. Liu, O. J. Lee, T. J. Gudmundsen, D. C. Ralph, and R. A. Buhrman, Current-Induced Switching of Perpendicularly Magnetized Magnetic Layers Using Spin Torque from the Spin Hall Effect, Phys. Rev. Lett. **109,** 096602 (2012).

[3] C. O. Avci, A. Quindeau, C. F. Pai, M. Mann, L. Caretta, A. S. Tang, M. C. Onbasli, C. A. Ross, and G. S. D. Beach, Current-induced switching in a magnetic insulator, Nat. Mater. **16,** 309 (2017).

[4] T. Kampfrath, A. Sell, G. Klatt, A. Pashkin, S. Mahrlein, T. Dekorsy, M. Wolf, M. Fiebig, A. Leitenstorfer, and R. Huber, Coherent terahertz control of antiferromagnetic spin waves, Nat. Photonics **5,** 31 (2011).

[5] X. Marti, I. Fina, C. Frontera, J. Liu, P. Wadley, Q. He, R. J. Paull, J. D. Clarkson, J. Kudrnovsky, I. Turek, J. Kunes, D. Yi, J. H. Chu, C. T. Nelson, L. You, E. Arenholz, S. Salahuddin, J. Fontcuberta, T. Jungwirth, and R. Ramesh, Room-temperature antiferromagnetic memory resistor, Nat. Mater. **13,** 367 (2014).

[6] J. Železný, P. Wadley, K. Olejník, A. Hoffmann, and H. Ohno, Spin transport and spin torque in antiferromagnetic devices, Nat. Phys. **14,** 220 (2018).

[7] V. Baltz, A. Manchon, M. Tsoi, T. Moriyama, T. Ono, and Y. Tserkovnyak, Antiferromagnetic spintronics, Rev. Mod. Phys. **90,** 015005 (2018).

[8] W. Zhang, M. B. Jungfleisch, W. J. Jiang, J. E. Pearson, A. Hoffmann, F. Freimuth, and Y. Mokrousov, Spin Hall Effects in Metallic Antiferromagnets, Phys. Rev. Lett. **113,** 196602 (2014).

[9] T. Jungwirth, X. Marti, P. Wadley, and J. Wunderlich, Antiferromagnetic spintronics, Nat. Nanotechnol. **11,** 231 (2016).

[10] S. Urazhdin and N. Anthony, Effect of Polarized Current on the Magnetic State of an Antiferromagnet, Phys. Rev. Lett. **99,** 046602 (2007).

[11] R. Cheng, J. Xiao, Q. Niu, and A. Brataas, Spin Pumping and Spin-Transfer Torques in Antiferromagnets, Phys. Rev. Lett. **113,** 057601 (2014).

[12] T. Satoh, R. Iida, T. Higuchi, M. Fiebig, and T. Shimura, Writing and reading of an arbitrary optical polarization state in an antiferromagnet, Nat. Photonics **9,** 25 (2015).

[13] V. Lopez-Dominguez, H. Almasi, and P. K. Amiri, Picosecond Electric-Field-Induced Switching of Antiferromagnets, Phys. Rev. Applied **11,** 024019 (2019).

[14] O. Gomonay, T. Jungwirth, and J. Sinova, High Antiferromagnetic Domain Wall Velocity Induced by Neel Spin-Orbit Torques, Phys. Rev. Lett. **117,** 017202 (2016).

[15] R. Cheng, D. Xiao, and A. Brataas, Terahertz Antiferromagnetic Spin Hall Nano-Oscillator, Phys. Rev. Lett. **116,** 207603 (2016).

[16] R. Zarzuela and Y. Tserkovnyak, Antiferromagnetic textures and dynamics on the surface of a heavy metal, Phys. Rev. B **95,** 180402 (2017).

[17] H. V. Gomonay and V. M. Loktev, Spin transfer and current-induced switching in antiferromagnets, Phys. Rev. B **81,** 144427 (2010).

[18] P. Wadley et al., Electrical switching of an antiferromagnet, Science **351,** 587 (2016).

[19] M. Meinert, D. Graulich, and T. Matalla-Wagner, Electrical Switching of Antiferromagnetic Mn_2Au and the Role of Thermal Activation, Phys. Rev. Applied **9,** 064040 (2018).

[20] X. F. Zhou, J. Zhang, F. Li, X. Z. Chen, G. Y. Shi, Y. Z. Tan, Y. D. Gu, M. S. Saleem, H. Q. Wu, F. Pan, and C. Song, Strong Orientation-Dependent Spin-Orbit Torque in Thin Films of the Antiferromagnet Mn_2Au Phys. Rev. Applied **9,** 054028 (2018).

[21] S. Y. Bodnar, L. Šmejkal, I. Turek, T. Jungwirth, O. Gomonay, J. Sinova, A. A. Sapozhnik, H. J. Elmers, M. Kläui, and M. Jourdan, Writing and reading antiferromagnetic Mn_2Au by Néel spin-orbit torques and large anisotropic magnetoresistance, Nat. Commun. **9,** 348 (2018).

[22] M. J. Grzybowski, P. Wadley, K. W. Edmonds, R. Beardsley, V. Hills, R. P. Campion, B. L. Gallagher, J. S. Chauhan, V. Novak, T. Jungwirth, F. Maccherozzi, and S. S. Dhesi, Imaging Current-Induced Switching of Antiferromagnetic Domains in CuMnAs, Phys. Rev. Lett. **118,** 057701 (2017).

[23] X. Z. Chen, R. Zarzuela, J. Zhang, C. Song, X. F. Zhou, G. Y. Shi, F. Li, H. A. Zhou, W. J. Jiang, F. Pan, and Y. Tserkovnyak, Antidamping-Torque-Induced Switching in Biaxial Antiferromagnetic Insulators, Phys. Rev. Lett. **120,** 207204 (2018).

[24] I. Gray, T. Moriyama, N. Sivadas, G. M. Stiehl, J. T. Heron, R. Need, B. J. Kirby, D. H. Low, K. C. Nowack, D. G. Schlom, D. C. Ralph, T. Ono, and G. D. Fuchs, Spin Seebeck Imaging of Spin-Torque Switching in Antiferromagnetic Pt/NiO Heterostructures Phys. Rev. X **9,** 041016 (2019).

[25] T. Moriyama, K. Oda, T. Ohkochi, M. Kimata, and T. Ono, Spin torque control of antiferromagnetic moments in NiO, Sci. Rep. **8,** 14167 (2018).

[26] L. Baldrati, O. Gomonay, A. Ross, M. Filianina, R. Lebrun, R. Ramos, C. Leveille, T. Forrest, F. Maccherozzi, E. Saitoh, J. Sinova, and M. Kläui, Mechanism of Néel Order Switching in Antiferromagnetic Thin Films Revealed by Magneto-transport and Direct Imaging, Phys. Rev. Lett. **123,** 177201 (2019).

[27] B. Peters, A. Alfonsov, C. G. F. Blum, S. J. Hageman, P. M. Woodward, S. Wurmehl, B. Büchner, and F. Y. Yang, Epitaxial films of Heusler compound $Co_2FeAl_{0.5}Si_{0.5}$ with high crystalline quality grown by off-axis sputtering, Appl. Phys. Lett. **103,** 162404 (2013).

[28] A. J. Lee, J. T. Brangham, Y. Cheng, S. P. White, W. T. Ruane, B. D. Esser, D. W. McComb, P. C. Hammel, and F. Y. Yang, Metallic ferromagnetic films with magnetic damping under 1.4×10^{-3} Nat. Commun. **8,** 234 (2017).

[29] F. Y. Yang and P. C. Hammel, Topical review: FMR-driven spin pumping in $Y_3Fe_5O_{12}$-based structures, J. Phys. D **51,** 253001 (2018).

[30] Y. Cheng, S. S. Yu, A. S. Ahmed, M. L. Zhu, Y. Rao, M. Ghazisaeidi, J. Hwang, and F. Y. Yang, Anisotropic

magnetoresistance and nontrivial spin Hall magnetoresistance in Pt/α-Fe$_2$O$_3$ bilayers, Phys. Rev. B **100,** 220408 (2019).

[31] Y. Cheng, S. S. Yu, M. L. Zhu, J. Hwang, and F. Y. Yang, Evidence of the Topological Hall Effect in Pt/Antiferromagnetic Insulator Bilayers, Phys. Rev. Lett. **123,** 237206 (2019).

[32] F. P. Chmiel, N. Waterfield Price, R. D. Johnson, A. D. Lamirand, J. Schad, G. van der Laan, D. T. Harris, J. Irwin, M. S. Rzchowski, C. B. Eom, and P. G. Radaelli, Observation of magnetic vortex pairs at room temperature in a planar α-Fe$_2$O$_3$/Co heterostructure, Nat. Mater. **17,** 581 (2018).

[33] R. Lebrun, A. Ross, S. A. Bender, A. Qaiumzadeh, L. Baldrati, J. Cramer, A. Brataas, R. A. Duine, and M. Kläui, Tunable long-distance spin transport in a crystalline antiferromagnetic iron oxide, Nature (London) **561,** 222 (2018).

[34] See Supplemental Material at http://link.aps.org/supplemental/10.1103/PhysRevLett.124.027202 for addition results of RHEED, SQUID, Monte Carlo simulation, and control measurements on Pt/Al$_2$O$_3$, Pt/SrTiO$_3$, and Pt/Cr$_2$O$_3$.

[35] A. H. Morrish, *Canted Antiferromagnetism: Hematite* (World Scientific, Singapore, 1994).

[36] T. Fujii, M. Takano, R. Kakano, Y. Isozumi, and Y. Bando, Spin-flip anomalies in epitaxial α-Fe$_2$O$_3$ films by Mössbauer spectroscopy, J. Magn. Magn. Mater. **135,** 231 (1994).

[37] S. Gota, M. Gautier-Soyer, and M. Sacchi, Magnetic properties of Fe$_2$O$_3$(0001) thin layers studied by soft x-ray linear dichroism, Phys. Rev. B **64,** 224407 (2001).

[38] L. Baldrati, O. Gomonay, A. Ross, M. Filianina, R. Lebrun, R. Ramos, C. Leveille, F. Fuhrmann, T. R. Forrest, F. Maccherozzi, S. Valencia, F. Kronast, E. Saitoh, J. Sinova, and M. Kläui, Mechanism of Neel Order Switching in Antiferromagnetic Thin Films Revealed by Magnetotransport and Direct Imaging, Phys. Rev. Lett. **123,** 177201 (2019).

[39] P. Chen, N. Lee, S. McGill, S. W. Cheong, and J. L. Musfeldt, Magnetic-field-induced color change in α-Fe$_2$O$_3$ single crystals, Phys. Rev. B **85,** 174413 (2012).

[40] L. Baldrati, A. Ross, T. Niizeki, C. Schneider, R. Ramos, J. Cramer, O. Gomonay, M. Filianina, T. Savchenko, D. Heinze, A. Kleibert, E. Saitoh, J. Sinova, and M. Klaui, Full angular dependence of the spin Hall and ordinary magnetoresistance in epitaxial antiferromagnetic NiO(001)/Pt thin films, Phys. Rev. B **98,** 024422 (2018).

[41] J. Fischer, O. Gomonay, R. Schlitz, K. Ganzhorn, N. Vlietstra, M. Althammer, H. Huebl, M. Opel, R. Gross, S. T. B. Goennenwein, and S. Geprägs, Spin Hall magnetoresistance in antiferromagnet/heavy-metal heterostructures, Phys. Rev. B **97,** 014417 (2018).

[42] C. C. Chiang, S. Y. Huang, D. Qu, P. H. Wu, and C. L. Chien, Absence of Evidence of Electrical Switching of the Antiferromagnetic Neel Vector, Phys. Rev. Lett. **123,** 227203 (2019).